

# Enriched contact finite elements for stable peeling computations

Roger A. Sauer <sup>1</sup>

*Aachen Institute for Advanced Study in Computational Engineering Science (AICES), RWTH Aachen University, Templergraben 55, 52056 Aachen, Germany*

Published<sup>2</sup> in the *International Journal for Numerical Methods in Engineering*, DOI: [10.1002/nme.3126](https://doi.org/10.1002/nme.3126)  
Submitted on 26 May 2010, Revised on 24 November 2010, Accepted on 8 December 2010

---

## Abstract

During peeling of a soft elastic strip from a substrate, strong adhesional forces act locally inside the peeling zone. It is shown here, that when a standard contact finite element formulation is used to compute the peeling process, a large mesh refinement is required since the numerical solution procedure becomes unstable otherwise. To improve this situation, several different efficient enrichment strategies are presented that provide stable solution algorithms for comparably coarse meshes. The enrichment is based on the introduction of additional unknowns inside the contact elements discretizing the slave surface. These are chosen in order to improve the approximation of the peeling forces while keeping the overall number of degrees of freedom low. If needed, these additional unknowns can be condensed out locally. The enrichment formulation is developed for both 2D and 3D nonlinear finite element formulations. The new enrichment technique is applied to the peeling computation of a gecko spatula. The proposed enriched contact element formulations are also investigated in sliding computations.

**Keywords:** adhesion, computational contact mechanics, nonlinear finite element methods, peeling, enhanced finite elements

---

## 1 Introduction

The understanding of the peeling behavior is central to many important applications in coating, bonding and adhesion technology. Examples include the bonding properties of thin films and the adhesion mechanisms of various insects and lizards. There is also a standardized peeling test used to analyze the properties of adhesives and adherents. Peeling is often compared to fracturing and therefore finite element based cohesive fracture models are often considered in peeling computations [1, 2, 3, 4]. A challenge in the computation of peeling problems are the large peeling stresses that can occur in a very narrow zone at the peeling front. Classical finite element (FE) based contact formulations often lead to a dilemma: Either a highly refined FE description is chosen, which is computationally expensive, or a coarse description is used, which is efficient but inaccurate and perhaps even unstable during computations. It therefore becomes desirable to develop improved computational contact formulations for peeling that are both accurate and efficient.

Such a formulation is proposed in this paper. The approach is based on a local enrichment of the contact surface such that the contact surface representation is more accurate than the bulk representation. Therefore, a new class of enhanced surface elements for contact are presented.

---

<sup>1</sup>email: [sauer@aices.rwth-aachen.de](mailto:sauer@aices.rwth-aachen.de)

<sup>2</sup>This pdf is a personal version of an article whose final publication is available at [www.onlinelibrary.wiley.com](http://www.onlinelibrary.wiley.com)

The simplest of these is the so-called Q1C2 element, which approximates the contact surface by a quadratic interpolation while the bulk is approximated by a linear interpolation. This element has the same contact accuracy as a fully quadratic finite element contact description (e.g. see [5]), but is much more efficient. The new elements are initially developed to improve peeling computations but they also show improved behavior for sliding computations. The approach is quite simple, efficient and very effective. The proposed contact enrichment technique shares similarities with enhanced assumed strain methods [6] and with the XFEM enrichment technique [7]. The new enrichment is particularly advantageous for contact problems where the accuracy is mainly governed by the accuracy of the contact description, rather than the accuracy of the bulk, as is often the case for peeling and sliding contact problems. The new approach is formulated in the framework of non-linear computational contact mechanics [8, 9]. The adhesive contact description is based on the formulation of [10], which is particularly suitable for adhesion at very small length scales.

The proposed surface enrichment approach bears some similarities with contact surface smoothing techniques that have been considered by several authors to describe contact with rigid bodies [11], 2D contact of general, deformable bodies [9, 12, 13, 14, 15, 16] and general 3D contact [17, 18, 19]. These methods have in common that they consider the smoothing of the master surface in order to improve the contact forces obtained through the projection of slave points onto the master surface. Furthermore, the smoothed surface description is not used in the FE bulk interpolation itself, which is instead based on usual Lagrange interpolation. In contrast to this, the presented work considers the smoothing of the slave surface in order to improve the accuracy of integration of the contact forces, and uses the smoothed surface description also in the bulk FE interpolation. Two surface enrichment strategies are presented, one based on p-refinement and one based on Hermite interpolation. The Hermite-based enrichment formulation proposed here, provides a  $C^1$  continuous contact surface description, resulting, as is shown, in a highly accurate contact element. High order continuous surface descriptions have shown several advantages in computational modeling [20]. The proposed enrichment technique is only considered on the surface and is therefore different from adaptive bulk enrichment approaches for delamination and contact problems, e.g. see [21]. The presented formulation is also different from surface enrichment techniques that have appeared recently for contact, using a different p-refinement approach [22], and cohesive zone models, using hierarchical enrichment functions [2, 23] and an enrichment based on an elastic foundation solution [24].

The remainder of this paper is structured as follows: Section 2 provides an overview of the computational contact approach used to describe adhesive contact. Section 3 illustrates the difficulty that can appear during peeling computations and proposes two different strategies to remove the problem in 2D. An extension to 3D is then considered in Section 4. Section 5 demonstrates the improved formulations on two applications. Section 6 concludes this paper.

## 2 Contact formulation for adhesion

This section presents an overview of the adhesion formulation in the framework of computational contact mechanics [8, 9]. The description is based on the large-deformation contact model developed in [10], which uses the Lennard-Jones potential to describe van der Waals adhesion, although in principle also other force-separation laws, like cohesive zone models [25], can be considered readily. First, the adhesion problem is outlined in the general continuum setting and then corresponding finite element formulations are discussed. The presentation focusses on quasi-static frictionless contact conditions.

### The adhesion problem

Consider two deformable solids  $\mathcal{B}_k$  ( $k = 1, 2$ )<sup>3</sup> with a given set of volumetric loads  $\bar{\mathbf{b}}_k$  in  $\mathcal{B}_k$ , surface loads  $\bar{\mathbf{t}}_k$  on  $\partial_t \mathcal{B}_k \subset \partial \mathcal{B}_k$  and prescribed deformation  $\bar{\boldsymbol{\varphi}}_k$  on  $\partial_\varphi \mathcal{B}_k \subset \partial \mathcal{B}_k$ . Assume that

$$\partial_\varphi \mathcal{B}_k \cup \partial_t \mathcal{B}_k = \partial \mathcal{B}_k \quad (1)$$

and

$$\partial_\varphi \mathcal{B}_k \cap \partial_t \mathcal{B}_k = \emptyset . \quad (2)$$

Further, consider a contact surface  $\partial_c \mathcal{B}_k \subset \partial_t \mathcal{B}_k$  on each body. On this surface both contact tractions  $\mathbf{T}_{ck}$  and non-zero external loads  $\bar{\mathbf{t}}_k$  may act together. Introducing the space of kinematically admissible deformations,

$$\mathcal{U}_k = \{ \mathbf{u}_k : \mathcal{B}_k \rightarrow \mathbb{R}^3 \mid \mathbf{u}_k = \bar{\boldsymbol{\varphi}}_k \text{ on } \partial_\varphi \mathcal{B}_k \} , \quad (3)$$

and the space of kinematically admissible variations,

$$\mathcal{V}_k = \{ \mathbf{v}_k : \mathcal{B}_k \rightarrow \mathbb{R}^3 \mid \mathbf{v}_k = 0 \text{ on } \partial_\varphi \mathcal{B}_k \} , \quad (4)$$

the weak form of the quasi-static contact adhesion problem is given by the following statement: Find  $\boldsymbol{\varphi}_k \in \mathcal{U}_k$  satisfying

$$\sum_{k=1}^2 \left[ \int_{\mathcal{B}_k} \text{grad}(\delta \boldsymbol{\varphi}_k) : \boldsymbol{\sigma}_k \, dv_k - \int_{\partial_c \mathcal{B}_{0k}} \delta \boldsymbol{\varphi}_k \cdot \mathbf{T}_{ck} \theta_k \, dA_k - \delta \Pi_{\text{ext},k} \right] = 0 , \quad \forall \delta \boldsymbol{\varphi}_k \in \mathcal{V}_k , \quad (5)$$

where

$$\delta \Pi_{\text{ext},k} = \int_{\mathcal{B}_k} \delta \boldsymbol{\varphi}_k \cdot \rho_k \bar{\mathbf{b}}_k \, dv_k + \int_{\partial_t \mathcal{B}_k} \delta \boldsymbol{\varphi}_k \cdot \bar{\mathbf{t}}_k \, da_k \quad (6)$$

is the virtual work of the prescribed external loads. In weak form (5), the Cauchy stress tensor  $\boldsymbol{\sigma}_k$  in  $\mathcal{B}_k$  is obtained from the constitutive model as a function of the deformation  $\boldsymbol{\varphi}_k$  of body  $\mathcal{B}_k$  (see Appendix A). The contact traction  $\mathbf{T}_{ck}$  is a vector in  $\mathbb{R}^3$ , that depends on the surface deformation  $\boldsymbol{\varphi}_k \in \partial \mathcal{B}_k$  of both bodies.

Remarks:

1. Weak form (5) can be derived from a variational principle [26, 27].
2. If one body is rigid, the sum and index  $k$  are dropped; this is considered in the following finite element description.
3. In eq. (5), the first term is written as an integral over the current configuration of the bodies,  $\mathcal{B}_k$ , while the second term is written as an integral of the reference configuration of the bodies  $\mathcal{B}_{0k}$ . This is advantageous in the FE implementation.
4. Due to the long-range nature of adhesion, even far away surface regions may experience significant contact forces, and in principle one may consider the entire surface  $\partial \mathcal{B}_k$  as the contact surface  $\partial_c \mathcal{B}_k$  [27].
5. Due to the decay of adhesion forces, a cut-off radius can be considered, so that the contact surface is reduced.
6. The scalar quantity  $\theta_k$  is related to the angle between the neighboring contact surfaces and is only significant if the adhesion is very strong, as is shown in [27]. For several practical applications, like gecko adhesion,  $\theta_k$  can be set to unity. This is considered in the following computations.

---

<sup>3</sup>In this treatment the symbol  $\mathcal{B}$  is used to denote both the body and the configuration it occupies in  $\mathbb{R}^3$ .

7. Looking at the weak form, the question arises how to compute the volume and surface integrals: Does it make sense to use the same accuracy for the two conceptually different integrals? It is shown in this paper, that it is highly advantageous to use different approaches.

In order to evaluate the contact traction  $\mathbf{T}_{ck}$ , the surface distance between the contacting bodies needs to be determined. Therefore, the closest point projection of the generic surface point  $\mathbf{x}_s \in \partial_c \mathcal{B}_k$  (which will correspond to a surface quadrature point in the discrete setting) onto the surface of the neighboring body,  $\mathcal{B}_\ell$  ( $\ell \neq k$ ), is computed. This computation yields the projection point  $\mathbf{x}_p \in \partial \mathcal{B}_\ell$ , and the surface distance at  $\mathbf{x}_s$  can be obtained from

$$r_s(\mathbf{x}_s) = \|\mathbf{x}_s - \mathbf{x}_p(\mathbf{x}_s)\| . \quad (7)$$

The projection direction is equal to the normal of the neighboring body at  $\mathbf{x}_p$ , which is denoted as  $\mathbf{n}_p$ , and is also a function of  $\mathbf{x}_s$ . In the following, two cases are considered: Van der Waals adhesion and the contact penalty method.

Van der Waals adhesion can be described by the function

$$\mathbf{T}_{ck}(\mathbf{x}_s) = T_c \mathbf{n}_p , \quad T_c(r_s) = \frac{A_H}{2\pi r_0^3} \left[ \frac{f_1}{45} \left( \frac{r_0}{r_s} \right)^9 - \frac{f_2}{3} \left( \frac{r_0}{r_s} \right)^3 \right] , \quad (8)$$

which is obtained from integrating the Lennard-Jones potential four times [10]. Here  $A_H$  is Hamaker's constant and  $r_0$  is the atomic equilibrium spacing of the Lennard-Jones potential. The coefficients  $f_1$  and  $f_2$  depend on the curvature of the neighboring body. If the adhesive substrate is flat, as is considered in the examples here,  $f_1 = f_2 = 1$  (see [27]). Figure 1.a displays the function  $T_c(r_s)$  given in eq. (8). It is characterized by the equilibrium distance

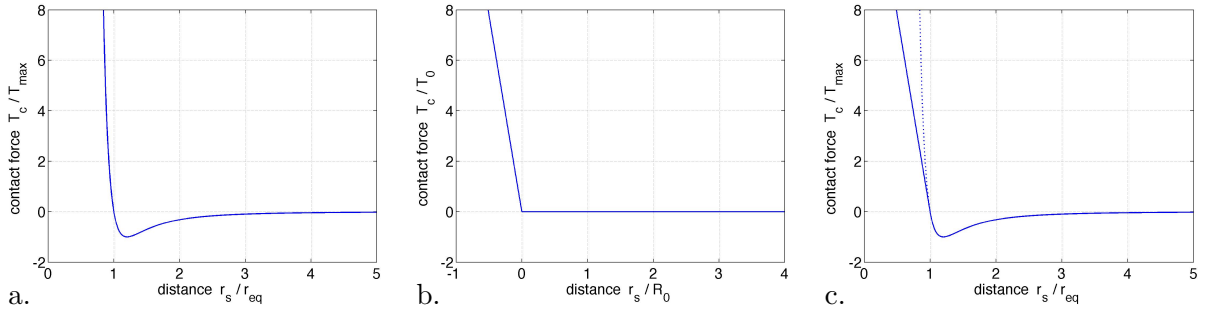


Figure 1: Contact force according to a. Van der Waals adhesion ; b. Penalty method; c. Regularized van der Waals adhesion.

$$r_{eq} = \sqrt[6]{1/15} r_0 , \quad (9)$$

where  $T_c = 0$ , the minimum

$$T_{\min} = T_c(r_{T\min}) = -\sqrt{5} \frac{A_H}{9\pi r_0^3} , \quad r_{T\min} = \sqrt[6]{1/5} r_0 = \sqrt[6]{3} r_{eq} , \quad (10)$$

which corresponds to the maximum possible attractive traction, and the work of adhesion

$$w_{adh} = - \int_{r_{eq}}^{\infty} T_c dr_s = \sqrt[3]{15} \frac{A_H}{16\pi r_0^2} , \quad (11)$$

which has the units J/m<sup>2</sup>. The maximum stiffness

$$k_{\text{adh}} = \max_{r_s} \frac{\partial T_c}{\partial r_s} = \sqrt[3]{4} \frac{3A_H}{10\pi r_0^4} \quad (12)$$

is also important, since it may cause an attractive instability during contact as is described in [10]. During adhesive contact the distance  $r_{\text{Tmin}}$  (and thus also the maximum tensile traction  $T_{\text{min}}$ ) is always attained on some surface region.

For comparison, Figure 1 also shows the contact force according to the penalty method, i.e.

$$\mathbf{T}_{ck}(\mathbf{x}_s) = -\epsilon_n r_s \mathbf{n}_p, \quad \text{if } r_s < 0, \quad \text{else } \mathbf{T}_{ck}(\mathbf{x}_s) = \mathbf{0} \quad (13)$$

where  $-r_s$  corresponds to the penetration of point  $\mathbf{x}_s$  into the neighboring body and  $\epsilon_n$  is the penalty parameter. An active set strategy is used to distinguish between active and inactive contact points. In case of adhesion (8), no active set strategy is needed, since all contact points are active (unless a cut-off radius is considered). One major difficulty of expression (8) is that highly refined finite element discretizations are required in order to resolve the attractive forces accurately. Coarse meshes lead to poor computational behavior and loss of convergence, which is the motivation for the new formulation addressed in this paper (see Section 3). A second difficulty of (8) is that the contact stiffness goes to infinity as one approaches  $r_s = 0$ . This can be fixed numerically by using a regularized force, where the slope is set to a constant value below a certain distance  $r_s$ , as is shown in Figure 1.c.

The finite element (FE) formulation follows from weak form (5). Considering a displacement based FE description the weak form is discretized into

$$\mathbf{v}^T [\mathbf{f}_{\text{int}} + \mathbf{f}_c - \mathbf{f}_{\text{ext}}] = \mathbf{0}, \quad \forall \mathbf{v} \in \mathcal{V}^h, \quad (14)$$

where  $\mathbf{f}$  and  $\mathbf{v}$  denote the forces and virtual displacements of the FE nodes. The first term denotes the internal virtual work that describes the bulk behavior. Details on the standard non-linear bulk FE formulation are provided in Appendix A. The second term captures the virtual work done by the contact forces. In view of eq. (5), the contact forces acting on the surface element  $\Gamma_0^e \in \partial_c \mathcal{B}_{0k}^h$  are

$$\mathbf{f}_c^e = - \int_{\Gamma_0^e} \mathbf{N}_e^T \mathbf{T}_{ck} dA, \quad (15)$$

where  $\mathbf{N}_e$  is the array

$$\mathbf{N}_e = [N_1 \mathbf{I}, N_2 \mathbf{I}, \dots, N_{n_{\text{se}}} \mathbf{I}] \quad (16)$$

that contains the  $n_{\text{se}}$  nodal shape functions used to interpolate the surface displacements (and the virtual surface displacements) as well as the geometry of the element. In 3D vector  $\mathbf{f}_c^e$  has the size  $(3n_{\text{se}} \times 1)$ . To simplify the evaluation, integral (15) is mapped to a simple master element  $\Gamma_{\square}$  following standard FE procedure. The bulk discretization is often based on bilinear quadrilateral elements for 2D problems and trilinear, 3D hexahedral elements for 3D problems (so called Q1 elements). On the surface one thus has linear, 1D elements or bilinear, 2D elements.<sup>4</sup> The corresponding master elements are a line segment of length 2, and a  $2 \times 2$  square. Numerical quadrature is used to integrate eq. (15) on the master domain, i.e.

$$\mathbf{f}_c^e \approx - \sum_{qp=1}^{n_{\text{qp}}} \mathbf{N}_e^T(\boldsymbol{\xi}_{qp}) \mathbf{T}_{ck}(\boldsymbol{\xi}_{qp}) j(\boldsymbol{\xi}_{qp}) w_{qp}, \quad \boldsymbol{\xi}_{qp} \in \Gamma_{\square}, \quad (17)$$

<sup>4</sup>The same nodes used to discretize the bulk are also used to discretize the surface.

where  $n_{qp}$  denotes the number of quadrature points,  $j$  denotes transformation of the surface area (according to  $dA = j w_{qp}$ ) and  $w_{qp}$  denotes the weight of the quadrature point. Further details, together with a closed-form expression of the contact stiffness matrix corresponding to force  $\mathbf{f}_c^e$  can be found in [28]. In the examples considered in this paper no external forces are considered ( $\mathbf{f}_{\text{ext}} = 0$ ).

### 3 2D enriched contact elements

This section discusses the numerical difficulty that appears during peeling computations. A new efficient enrichment strategy is presented that solves this problem. The enrichment is based on local p-refinement and Hermite polynomials. The 2D case is considered first.

#### 3.1 Numerical difficulties in peeling computations

In peeling computations a numerical difficulty appears for strong adhesion, which is illustrated by the following simple 2D test case: Consider a strip with length  $\ell = 200 L_0$  and height  $h = 10 L_0$  adhering to a rigid substrate. The strip is peeled off the substrate by applying a rotation  $\theta$  at the right boundary, as is shown in Figure 2.a. A rotation is chosen since it yields

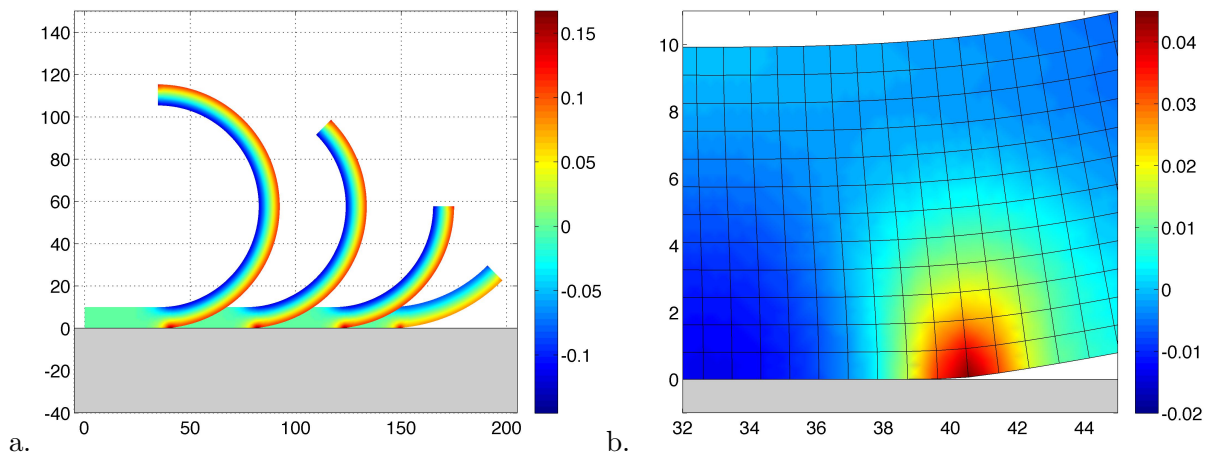


Figure 2: a. Peeling of a 2D elastic strip (coloring represents stress  $I_1 = \text{tr}\boldsymbol{\sigma}/E$ ); b. Delamination stress  $\sigma_{33}/E$ .

a constant moment during peeling. The strip is modeled by an isotropic, nonlinearly elastic Neo-Hooke material with  $E = 2 \text{ GPa}$  and  $\nu = 0.2$ . Plain strain conditions are considered. 12 elements are chosen over the strip height  $h$ . Adhesive contact is considered along 75% of the bottom surface (from  $x = 0$  to  $x = 150 L_0$ ), and the contact forces are described according to eq. (8), using  $r_0 = 0.4 \text{ nm}$  and  $A_H = 10^{-19} \text{ J}$ , which are the values associated with gecko adhesion.<sup>5</sup> The length is set to  $L_0 = 1 \text{ nm}$ , so that the strip height approximately corresponds to that of a gecko spatula [29]. At the delamination front large tensile stresses act on the strip as can be seen from Figure 2.b, which shows the vertical stress component  $\sigma_{33}$ . For the considered

<sup>5</sup> Remark: The contact force  $\mathbf{T}_{ck}$  is modified according to Figure 1.c: the slope is kept constant for  $r_s < 1.05r_{\text{eq}}$ . This corresponds to a penalty stiffness of  $1.95E/L_0$  and a maximum penetration of  $0.01 \text{ nm}$  w.r.t.  $r_{\text{eq}}$  for the contact pressures observed in Figure 2.b.

parameters the delamination zone is very small, and a very fine FE discretization is required to resolve this zone.

From a certain rotation angle onward, the bending moment  $M$ , required to impose the rotation  $\theta$ , will remain constant, as is seen in Figure 3.a. The enlargement in Figure 3.b, however, shows

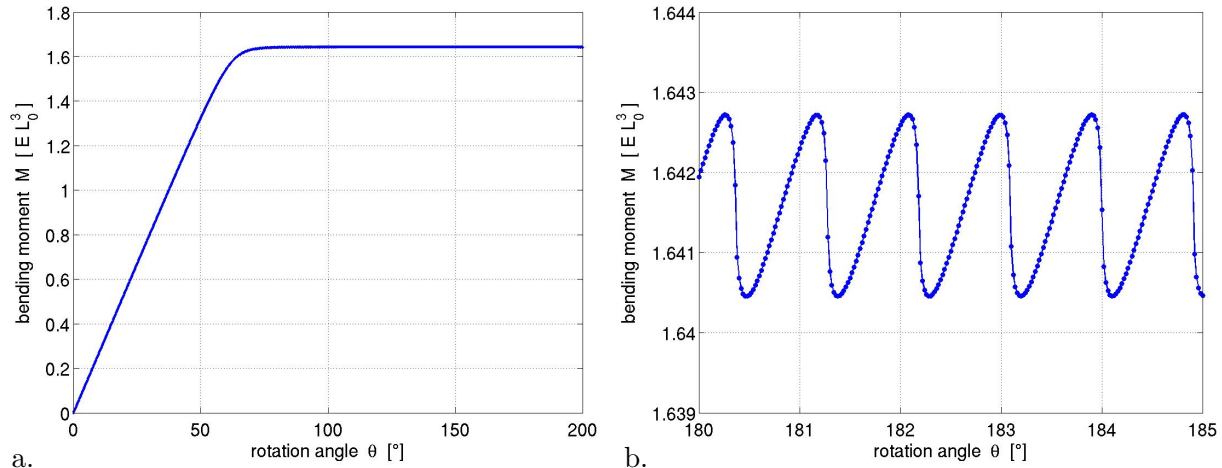


Figure 3: Bending moment  $M(\theta)$  for the peeling problem.

that the computed bending moment is not exactly constant but rather oscillates around a mean value. This oscillation strongly affects the convergence rate during the Newton-Raphson iteration used to solve this nonlinear problem. Especially the large negative slopes can lead to poor convergence and loss of convergence even though the oscillations only occur in the third decimal. Typically, the convergence rate alternates between faster and slower convergence (with the same wavelength as the moment oscillations). The convergence behavior may actually improve for a larger rotation step sizes,  $\Delta\theta$ , since for large steps one may jump over the stretches where the slope is very steep.

The oscillation error is due to the discretization error in the contact forces; refining the mesh will reduce its amplitude and wavelength (as is shown in Section 3.4.2). However, this will also increase the computational cost substantially, unless an adaptive refinement is considered at the delamination front. This on the other hand requires remeshing strategies, which are not trivial, especially in 3D. Here, we are rather interested in a simpler and efficient way to reduce the oscillation error. In the following sections two novel FE formulations are presented that achieve this. The oscillation problem also occurs in sliding computations and the new FE formulations also reduce the oscillation error there, as is shown in Section 5.2. Oscillations due to discretization error can also be observed during nanoindentation computations [30].

### 3.2 Surface enrichment based on p-refinement

The inaccuracies reported above result from the poor approximation of the surface traction (8) and its integration (15) for coarse surface meshes. Hence, it would be useful to improve the accuracy of the surface description. The first idea, therefore, consists of a simple p-refinement of the contact surface as is shown in Figure 4. This formulation can be developed from the

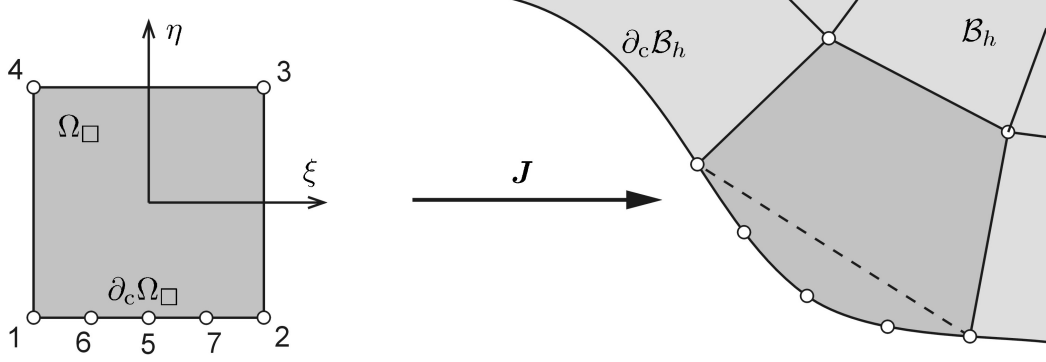


Figure 4: Surface enrichment based on p-refinement: Enhanced contact element Q1C4 and its map to the current domain.

standard 4-node quadrilateral, the Q1 element, which has the shape functions

$$\begin{aligned}
 N_1^0 &= \frac{1}{4}(1 - \xi)(1 - \eta) , \\
 N_2^0 &= \frac{1}{4}(1 + \xi)(1 - \eta) , \\
 N_3^0 &= \frac{1}{4}(1 + \xi)(1 + \eta) , \\
 N_4^0 &= \frac{1}{4}(1 - \xi)(1 + \eta) ,
 \end{aligned} \tag{18}$$

to interpolate the displacement field<sup>6</sup> according to

$$\mathbf{u}_e^h = \sum_{I=1}^4 N_I^0 \mathbf{u}_I . \tag{19}$$

If an additional fifth node is placed at  $\xi = 0, \eta = -1$ , the modifications

$$\begin{aligned}
 N_5 &= \frac{1}{2}(1 - \xi^2)(1 - \eta) , \\
 N_1 &= N_1^0 - \frac{1}{2}N_5 , \\
 N_2 &= N_2^0 - \frac{1}{2}N_5 ,
 \end{aligned} \tag{20}$$

are obtained [31].  $N_3$  and  $N_4$  remained unchanged. In the interior of the element, the displacement field now becomes

$$\mathbf{u}_e^h = \sum_{I=1}^5 N_I \mathbf{u}_I . \tag{21}$$

On the contact surface, considered at  $\eta = -1$ , this can be simplified into

$$\mathbf{u}_e^h = \sum_{I=1,2,5} N_I \mathbf{u}_I . \tag{22}$$

This element is combined with a standard Q1 formulation within the bulk, so that the interpolation is linear in the bulk and quadratic on the surface. In the first element layer a transition

<sup>6</sup>In the following description,  $\mathbf{u}$  and  $\mathbf{u}^h$  are used to denote the displacement field and its FE approximation,  $\mathbf{u}_e^h$  is used to denote the approximate displacement field inside element  $\Omega_e$ ,  $\mathbf{u}_I$  is used to denote the value of the displacement at node  $I$ ,  $\mathbf{u}^e$  is used to denote the stacked vector of all nodal displacements of element  $\Omega_e$ , and  $\mathbf{u}$  is used to denote the stacked vector of all nodal displacements of body  $\mathcal{B}^h$ . Analogous definitions are used for the reference configuration and the current configuration (characterized by the vector fields  $\mathbf{X}$  and  $\mathbf{x}$ ). Note that italic font is used for field variables and normal font is used for discrete variables.

zone exists, (where the formulation is still quadratic, due to the influence of the surface nodes). Formally this is written as

$$\begin{aligned} \mathbf{u}^h &\in \mathcal{P}^1 && \text{in } \mathcal{B}^h, \\ \mathbf{u}^h &\in \mathcal{P}_s^2 && \text{on } \partial_c \mathcal{B}^h, \end{aligned} \quad (23)$$

where  $\mathcal{P}^1$  denotes the space of continuous, piecewise linear functions (bilinear to be precise) and  $\mathcal{P}^2$  denotes the space of continuous, piecewise quadratic functions, i.e.

$$\begin{aligned} \mathcal{P}^p &:= \{ \mathbf{u}|_{\Omega_e} \in \mathcal{Q}^p \quad \forall \Omega_e \in \mathcal{B}^h \} && \text{with } \mathcal{Q}^p := \{ \mathbf{u}(\xi, \eta) = \sum_{0 \leq i, j \leq p} \mathbf{c}_{ij} \xi^i \eta^j \} && \text{in } \mathcal{B}^h, \\ \mathcal{P}_s^p &:= \{ \mathbf{u}|_{\Gamma_e} \in \mathcal{Q}_s^p \quad \forall \Gamma_e \in \partial \mathcal{B}^h \} && \text{with } \mathcal{Q}_s^p := \{ \mathbf{u}(\xi) = \sum_{0 \leq i \leq p} \mathbf{c}_i \xi^i \} && \text{on } \partial \mathcal{B}^h, \end{aligned} \quad (24)$$

for some coefficients  $c_i$  and  $c_{ij}$  [32]. The enriched 5-node quadrilateral satisfies the compact support property

$$N_a(\xi_b, \eta_b) = \delta_{ab}, \quad (25)$$

at the nodes, and the partition of unity

$$\sum_{I=1}^5 N_I = 1 \quad \forall \xi, \eta. \quad (26)$$

Since the element is linear in the bulk and quadratic on the contact surface, it is denoted as Q1C2 in the following. With this notation a standard displacement based contact formulation is a Q1C1 finite element formulation. Since each node has two dofs, the Q1C2 element has 10 dofs in total.

Another example of the p-refinement of the contact surface is the Q1C4 element (see Figure 4), an enriched 7-node quadrilateral with extra nodes at  $(\xi, \eta) = (0, -1)$ ,  $(-0.5, -1)$  and  $(0.5, -1)$ , that has the additional three shape function

$$\begin{aligned} N_5 &= 2(\xi^4 - \frac{5}{4}\xi^2 + \frac{1}{4})(1 - \eta), \\ N_6 &= -\frac{4}{3}(\xi^4 - \frac{1}{2}\xi^3 - \xi^2 + \frac{1}{2}\xi)(1 - \eta), \\ N_7 &= -\frac{4}{3}(\xi^4 + \frac{1}{2}\xi^3 - \xi^2 - \frac{1}{2}\xi)(1 - \eta), \end{aligned} \quad (27)$$

and the modifications

$$\begin{aligned} N_1 &= N_1^0 - \frac{1}{2}N_5 - \frac{3}{4}N_6 - \frac{1}{4}N_7, \\ N_2 &= N_2^0 - \frac{1}{2}N_5 - \frac{1}{4}N_6 - \frac{3}{4}N_7. \end{aligned} \quad (28)$$

For a FE mesh composed of Q1C4 elements on the contact surface and Q1 elements elsewhere, one thus has

$$\begin{aligned} \mathbf{u}^h &\in \mathcal{P}^1 && \text{in } \mathcal{B}^h, \\ \mathbf{u}^h &\in \mathcal{P}_s^4 && \text{on } \partial_c \mathcal{B}^h. \end{aligned} \quad (29)$$

Again, a transition zone exists within the surface elements. It can be confirmed that the Q1C4 element also satisfies the compact support property (25) and the partition of unity (26). The Q1C4 element has 14 dofs in total.

In principle also higher p-enriched elements can be formulated. The notation Q1Cp is used to denote a linear approximation in the bulk and a p-degree approximation on the surface. In 2D this element contains p + 1 surface nodes and has 2p + 6 dofs. The number of quadrature points must be increased along with the polynomial degree. In general also QqCp elements can be formulated with any q and p. Useful for contact is p > q. However, one should be aware of the Gibbs-oscillations that can occur for high order interpolation (see Section 5.2).

The enrichment formulation, which is formulated here for quadrilateral elements, can also be extended to triangular or other elements.

The computation of the internal force vector  $\mathbf{f}_{\text{int}}$  and the contact force vector  $\mathbf{f}_c$ , as well as the corresponding stiffness matrices  $\mathbf{k}_{\text{int}}$  and  $\mathbf{k}_c$ , follows from the same procedure as for the standard Q1 element by simply adjusting the number of nodes in the sums required to compute the deformation gradient  $\mathbf{F} = \frac{\partial \mathbf{x}}{\partial \mathbf{X}}$  and the Jacobian matrix  $\mathbf{J} = \frac{\partial \mathbf{x}}{\partial \boldsymbol{\xi}}$  and adjusting the matrix size of  $\mathbf{f}_{\text{int}}$ ,  $\mathbf{f}_c$ ,  $\mathbf{k}_{\text{int}}$  and  $\mathbf{k}_c$ ; see Appendix A.

In 2D, one can easily perform the static condensation of the additional enrichment unknowns at the element level, see [6]. The advantage of this is that the enrichment unknowns do not need to be considered in the global equation system.

### 3.3 Surface enrichment based on Hermite interpolation

The second enrichment idea consists of using a Hermite interpolation along the contact surface such that the interpolation becomes  $C^1$  continuous on the surface. Such an element has six nodes: four standard nodes for approximating the displacement and two additional surface nodes approximating the surface derivative (see Figure 5).

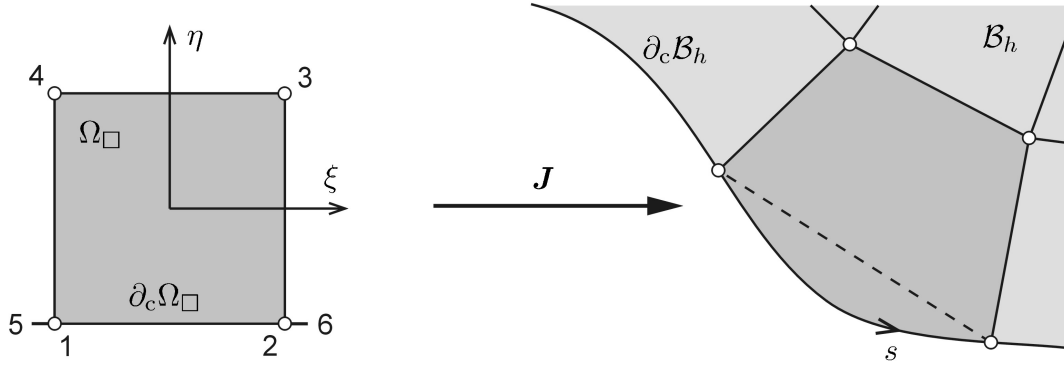


Figure 5: Surface enrichment based on Hermite interpolation: Enhanced contact element Q1CH and its map to the current domain.

The Hermite smoothed 6-noded quadrilateral is given by the FE interpolation

$$\mathbf{u}_e^h = \sum_{I=1}^4 N_I \mathbf{u}_I + \sum_{I=1}^2 H_I \mathbf{u}_{I,\xi} \quad (30)$$

and the Hermite shape functions

$$\begin{aligned} N_1(\xi, \eta) &= \frac{1}{8}(\xi - 1)^2(2 + \xi)(1 - \eta) , \\ N_2(\xi, \eta) &= \frac{1}{8}(\xi + 1)^2(2 - \xi)(1 - \eta) , \end{aligned} \quad (31)$$

and

$$\begin{aligned} H_1(\xi, \eta) &= \frac{1}{8}(\xi + 1)(\xi - 1)^2(1 - \eta) , \\ H_2(\xi, \eta) &= \frac{1}{8}(\xi + 1)^2(\xi - 1)(1 - \eta) . \end{aligned} \quad (32)$$

Shape functions  $N_3$  and  $N_4$  are the same as for the standard quadrilateral (18). Interpolation (30) satisfies the compact support property (25) and the partition of unity to represent constant

$\mathbf{u}_e^h$  and constant  $\mathbf{u}_{e,\xi}^h$ , i.e.

$$\sum_{I=1}^4 N_I \mathbf{u}_I + \sum_{I=1}^2 H_I \mathbf{u}_{I,\xi} = 1 \quad \forall \xi, \eta \quad (33)$$

for  $\mathbf{u}_I = 1$  and  $\mathbf{u}_{I,\xi} = 0$  and

$$\sum_{I=1}^4 N_{I,\xi} \mathbf{u}_I + \sum_{I=1}^2 H_{I,\xi} \mathbf{u}_{I,\xi} = 1 \quad \forall \xi, \eta \quad (34)$$

for  $\mathbf{u}_1 = \mathbf{u}_4 = c - 1$ ,  $\mathbf{u}_2 = \mathbf{u}_3 = c + 1$  and  $\mathbf{u}_{I,\xi} = 1$ , where  $c$  is an arbitrary constant.

At the contact surface  $\eta = -1$ , so that then

$$\mathbf{u}_e^h = \sum_{I=1}^2 (N_I \mathbf{u}_I + H_I \mathbf{u}_{I,\xi}) , \quad (35)$$

which is the usual Hermite interpolation in 1D, e.g. see [33]. The additional degrees of freedom introduced by  $H_1$  and  $H_2$  correspond to a nodal enrichment at node 1 and 2, which is marked by two short horizontal lines in Figure 5. This enrichment bears some resemblance to the nodal enrichment considered by the XFEM [7]. The new contact FE formulation according to eq. (30) is denoted as Q1CH3, or Q1CH in short, since the displacement field is interpolated by third order Hermite polynomials along the contact surface. The Q1CH element has 12 dofs in total. This element is combined with a standard Q1 formulation within the bulk. Hence the interpolated displacement field  $\mathbf{u}^h$  is continuous ( $C^0$ ) in the entire domain,  $\mathcal{B}^h$ , and continuously differentiable ( $C^1$ ) on the entire contact surface,  $\partial_c \mathcal{B}^h$ , i.e.

$$\begin{aligned} \mathbf{u}^h &\in C^0 \quad \forall \mathbf{x} \in \mathcal{B}^h , \\ \mathbf{u}^h &\in C^1 \quad \forall \mathbf{x} \in \partial_c \mathcal{B}^h . \end{aligned} \quad (36)$$

According to the isoparametric concept, the Hermite interpolation (30) is also used to approximate the element configuration itself, i.e.

$$\mathbf{X}_e^h = \sum_{I=1}^4 N_I \mathbf{X}_I + \sum_{I=1}^2 H_I \mathbf{X}_{I,\xi} , \quad (37)$$

for the undeformed reference configuration and similarly for the current configuration  $\mathbf{x}_e^h$ .

The nodal displacement derivatives  $\mathbf{u}_{I,\xi}$ , which refer to the master element coordinate system, can be transformed to the reference coordinate system according to

$$\mathbf{u}_{I,\xi} = \frac{\partial S}{\partial \xi} \mathbf{u}_{I,S} , \quad (38)$$

where  $S$  denotes the arc length along the reference configuration of the contact surface  $\partial_c \mathcal{B}_0$ . Thus eq. (30) becomes

$$\mathbf{u}_e^h = \sum_{I=1}^4 N_I \mathbf{u}_I + \sum_{I=1}^2 H_I \frac{\partial S}{\partial \xi} \mathbf{u}_{I,S} . \quad (39)$$

Here  $\mathbf{u}_{I,S}$  is the nodal value describing the derivative of  $\mathbf{u}^h$  along the reference surface such that

$$\left. \frac{\partial \mathbf{u}^h}{\partial S} \right|_{\mathbf{x}_I \in \partial \mathcal{B}} = \mathbf{u}_{I,S} , \quad (40)$$

similarly to the nodal identity

$$\mathbf{u}^h(\mathbf{X}_I) = \mathbf{u}_I . \quad (41)$$

Here in 2D,

$$\frac{\partial S}{\partial \xi} = \frac{L_c}{2} , \quad (42)$$

where  $L_c$  is the surface distance between nodes 1 and 2 in the reference configuration. It is more natural to prescribe  $\mathbf{u}_{I,S}$  instead of  $\mathbf{u}_{I,\xi}$ . The nodes of the current configuration are updated according to

$$\mathbf{x}_I = \mathbf{X}_I + \mathbf{u}_I \quad \text{and} \quad \mathbf{x}_{I,S} = \mathbf{X}_{I,S} + \mathbf{u}_{I,S} , \quad (43)$$

where  $\mathbf{u}_I$  and  $\mathbf{u}_{I,S}$  are obtained from solving the FE equilibrium equation. For the peeling example in Section 3.1,  $S$  runs parallel to  $\mathbf{e}_1$ , so that

$$\mathbf{X}_{I,S} = \mathbf{e}_1 \quad \forall I . \quad (44)$$

Given (39), the displacement gradient follows as

$$\frac{\partial \mathbf{u}_e^h}{\partial \mathbf{x}} = \sum_{I=1}^4 \mathbf{u}_I \otimes \frac{\partial N_I}{\partial \mathbf{x}} + \sum_{I=1}^2 \mathbf{u}_{I,S} \frac{\partial S}{\partial \xi} \otimes \frac{\partial H_I}{\partial \mathbf{x}} , \quad (45)$$

with

$$\frac{\partial N_I}{\partial \mathbf{x}} = \frac{\partial \xi}{\partial \mathbf{x}} \frac{\partial N_I}{\partial \xi} \quad \text{and} \quad \frac{\partial H_I}{\partial \mathbf{x}} = \frac{\partial \xi}{\partial \mathbf{x}} \frac{\partial H_I}{\partial \xi} , \quad (46)$$

where  $\frac{\partial \xi}{\partial \mathbf{x}} = \mathbf{J}^{-1}$  is given by eq. (55) in Appendix A. It is convenient to denote  $N_5 := H_1$ ,  $N_6 := H_2$  and  $\mathbf{u}_5 := \mathbf{u}_{1,\xi}$ ,  $\mathbf{u}_6 := \mathbf{u}_{2,\xi}$ , so that eqs. (30) and (45) can be simply written as

$$\mathbf{u}_e^h = \sum_{I=1}^6 N_I \mathbf{u}_I \quad \text{and} \quad \frac{\partial \mathbf{u}_e^h}{\partial \mathbf{x}} = \sum_{I=1}^6 \mathbf{u}_I \otimes \frac{\partial N_I}{\partial \mathbf{x}} . \quad (47)$$

With this notation one can use the same computational element routine as for the Q1Cp element, using only minor adjustments, see Appendix B.

Figure 6 shows the improvement in the surface deformation achieved by the Q1CH element. The improvement is particularly large at the delamination zone where it is needed most, and one can therefore expect a significant improvement resulting from this formulation. This is demonstrated in Section 3.4.2 and Section 5. Figure 6 also shows that the contact enrichment is only needed in a short surface region consisting of three to five surface elements. Thus an adaptive enrichment strategy can be used that moves the zone of enriched elements along with the peeling front.

The formalism presented above can also be used to derive an enhanced contact element that is  $C^2$  on the surface (the Q1CH5 element). One can also combine the p enrichment and the Hermite enrichment strategies.

### 3.4 Comparison

This section analyzes the computational performance of the new enhanced contact elements.

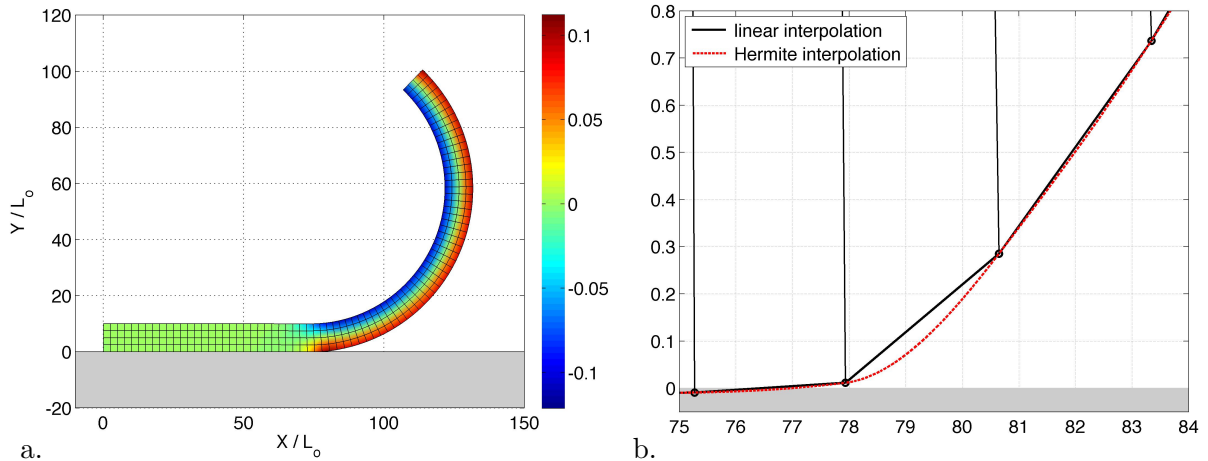


Figure 6: Surface smoothing achieved by the Q1CH element in the peeling example described in Section 3.1: a. Deformed configuration obtained with only four elements over the height; b. Enlargement of a. at the peeling front.

### 3.4.1 Bending performance

During peeling large bending deformations can occur and it therefore becomes important to analyze the FE accuracy for bending. We consider the strip of Section 3.1, subject it to pure bending (without considering any contact) and compare the convergence behavior of the new element formulations Q1C2, Q1C4 and Q1CH. For reference we also include the behavior of the bilinear Q1 element and the nonlinear enhanced strain element Q1E4 [6], which is very accurate in bending. In many applications only a small surface region may need a contact enrichment. To account for this, not all surface elements are enriched and only a short patch covering a. 75% and b. 10% of the bottom surface is modeled with the new contact elements. Altogether six cases are considered that are obtained by combining the enhanced contact elements with standard elements (see Table 1). The performance of these six cases is shown in Figure 7. The

case	surface elements	remaining elements
1	Q1	Q1
2	Q1	Q1E4
3	Q1C2	Q1E4
4	Q1CH	Q1E4
5	Q1C4	Q1E4
6	Q1E4	Q1E4

Table 1: FE formulations considered in the pure bending example.

figure shows that the bending performance of the new enhanced contact elements is much better than that of the Q1 element. The new elements perform almost equally well. The accuracy ranking corresponds to the order given in Table 1. The ‘error’ shown in Figure 7 is measured relative to a highly accurate solution obtained with the Q1E4 formulation on a fine mesh with  $m = 5$ . Further, during mesh refinement the relative number of enhanced contact elements (denoted Q1CX collectively) decreases (see Table 2), so that the rate of convergence quickly approaches that of the Q1E4 formulation. The relative decrease of the Q1CX elements shown in Table 2, also implies that the computational cost between standard and enriched formulation becomes less significant during mesh refinement. The example shows that the new contact

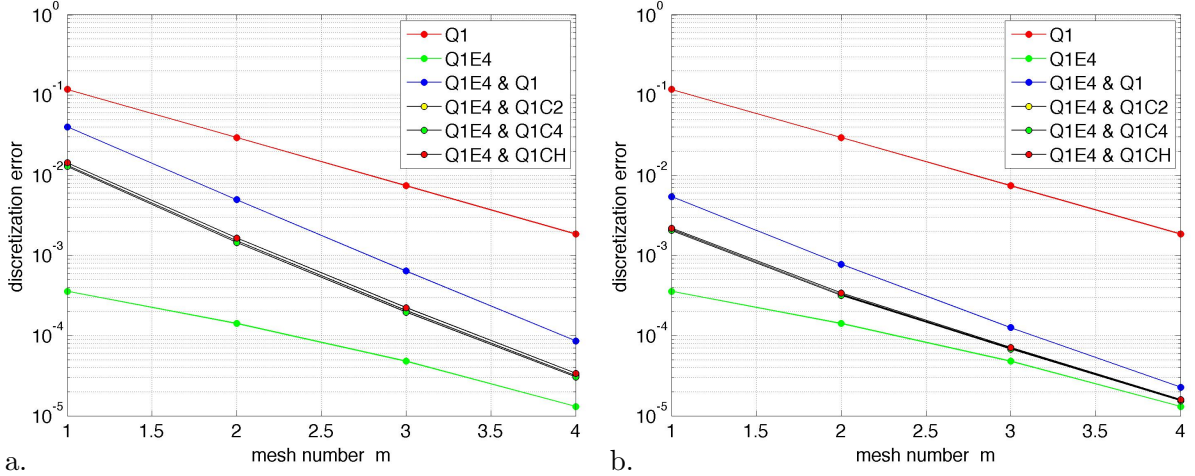


Figure 7: Discretization error of the different enrichment formulations during pure bending. Ratio of the bottom surface covered by Q1CX elements: a. 75%; b. 10%;  $2^m$  is the number of elements across the height of the strip.

mesh	$n_{el}$	$n_{cel}$ for 75%	$n_{cel}$ for 10%
$m = 1$	80	30 (37.5%)	4 (5%)
$m = 2$	320	60 (18.25%)	8 (2.5%)
$m = 3$	1280	120 (9.38%)	16 (1.25%)
$m = 4$	5120	240 (4.69%)	32 (0.63%)

Table 2: Number of contact elements  $n_{cel}$  compared to the number of total elements  $n_{el}$  for 75% and 10% surface coverage in the pure bending example.

elements will not cause locking in bending.

In principle the enhanced contact element formulation can also be combined with a enhanced strain element formulation like the Q1E4 element. The results of Figure 7 indicate that this would only be important if few elements over the thickness are used, e.g. in solid-shell formulations.

### 3.4.2 Peeling analysis

We now revisit the peeling example of Section 3.1 and report the improved accuracy obtained with the contact formulations Q1C2, Q1C4 and Q1CH, developed in Section 3.2 and 3.3. For the analysis we examine the oscillations in the moment-rotation curve shown in Figure 3. In theory there should be no oscillations, as the moment is constant.<sup>7</sup> The oscillation error is characterized by the amplitude  $\Delta M$ , by the average moment  $\text{ave}(M)$ , by the wavelength  $\Delta\theta$  and the maximum, minimum and average values of the slope  $M_{,\theta} = \partial M / \partial \theta$ . Table 3 shows the numeric values obtained for three different meshes, considering  $n_y = 8, 12$  and 16 elements across the strip height.

One can observe a substantial decrease of  $\Delta M$  and  $M_{,\theta}$ . This is also shown in Figure 8. Thus, the enriched contact elements are much more accurate in peeling than the original Q1C1 contact formulation. The relative improvement for  $n_y = 12$  elements is shown in Table 4. Compared

<sup>7</sup>Considering linear beam theory, this problem can be solved analytically [34].

element	$n_y$	$\Delta M$	$\Delta\theta$	$\max(M_\theta)$	$\min(M_\theta)$	$\text{ave}(M_\theta)$	$\text{ave}(M)$
Q1C1	8	–	–	–	–	–	–
Q1C2	8	4.612e-03	1.363e+00	5.539e-03	-1.003e-01	8.3872e-07	1.641467e+00
Q1C4	8	1.798e-03	1.363e+00	2.998e-03	-6.619e-03	8.3425e-07	1.641475e+00
Q1CH	8	1.011e-03	1.364e+00	1.689e-03	-3.597e-03	8.2969e-07	1.641532e+00
Q1C1	12	2.267e-03	9.081e-01	4.699e-03	-2.355e-02	9.5827e-07	1.641565e+00
Q1C2	12	6.082e-04	9.090e-01	1.806e-03	-2.461e-03	9.1761e-07	1.641406e+00
Q1C4	12	2.283e-04	9.090e-01	7.553e-04	-7.978e-04	9.1759e-07	1.641402e+00
Q1CH	12	1.491e-04	9.090e-01	4.795e-04	-5.621e-04	9.1731e-07	1.641411e+00
Q1C1	16	2.684e-04	6.812e-01	1.131e-03	-1.385e-03	9.8713e-07	1.641449e+00
Q1C2	16	9.144e-05	6.815e-01	3.958e-04	-4.388e-04	9.8360e-07	1.641384e+00
Q1C4	16	4.050e-05	6.815e-01	1.764e-04	-1.902e-04	9.8371e-07	1.641383e+00
Q1CH	16	2.031e-05	6.819e-01	9.277e-05	-9.508e-05	9.8375e-07	1.641386e+00

Table 3: Analysis of the peeling moment for the various element formulations.

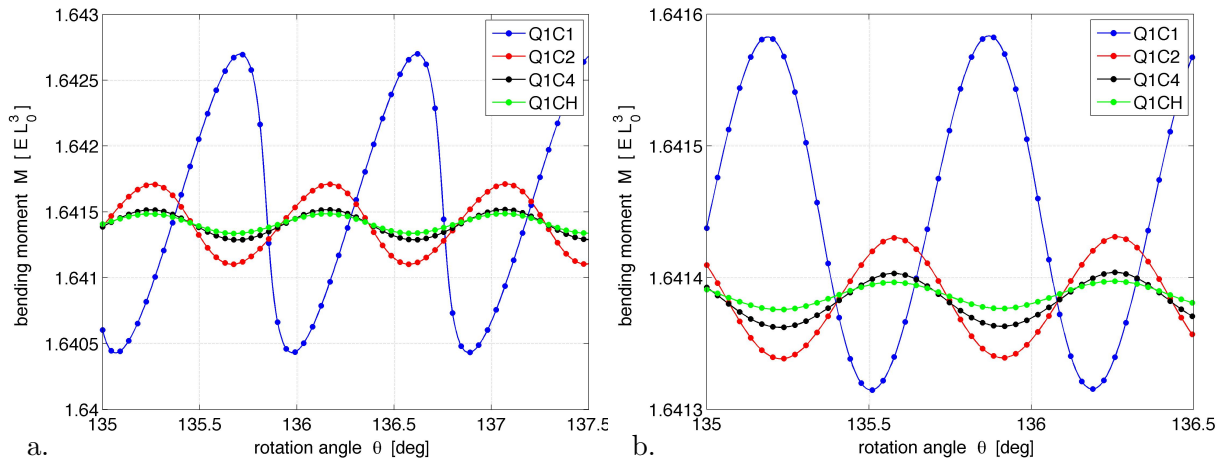


Figure 8: Improvement due to the different contact enrichments for: a.  $n_y = 12$  elements along the strip height  $h$ ; b.  $n_y = 16$  elements along  $h$ .

to the Q1C1 formulation, the oscillation error reduces by a factor of 3.7 for the Q1C2, by a factor 10 for the Q1C4 and by a factor of 15 for the Q1CH formulation! The reduction of the downward slope, critical for convergence, is even more pronounced, as the table shows. In order to obtain highly accurate results, 50 equidistant quadrature points are used for evaluating (17). The reduction of the oscillation amplitudes and slopes lead to a more robust computational performance that requires less Newton iteration steps. The case for  $n_y = 8$  does not even converge for the original Q1C1 contact formulation. The wavelength of the oscillations is equal for all formulations since it only depends on the mesh size. Table 3 shows that a simple h-refinement will also decrease the oscillation error substantially. However, a uniform h-refinement is very expensive, and an adaptive h-refinement is non-trivial, especially in 3D.

The major advantage of the enhanced contact element formulation is that no remeshing step is required: The Q1C2, the Q1C4 and the Q1CH formulations use the same mesh as the standard Q1C1 formulation.

contact formulation	oscillation error	downward slope error
Q1C1	100%	100%
Q1C2	26.8%	10.5%
Q1C4	10.1%	3.39%
Q1CH	6.58%	2.39%

Table 4: Improvement achieved by the new contact elements: Reduction of the oscillation error  $\Delta M$  and the downward slope error  $\min(M_{,\theta})$  for  $n_y = 12$  compared to the Q1C1 formulation.

## 4 3D contact enrichment elements based on p-refinement

Due to the success of the contact enrichment in 2D, we now extend the concept to 3D and demonstrate its improvement on an important application. We therefore consider the extension of the Q1C2 element presented in Section 3.2 to 3D. To satisfy property (23) in 3D, the Q1C2 element requires 9 nodes on the contact surface and 4 nodes in the interior as shown in Figure 9.

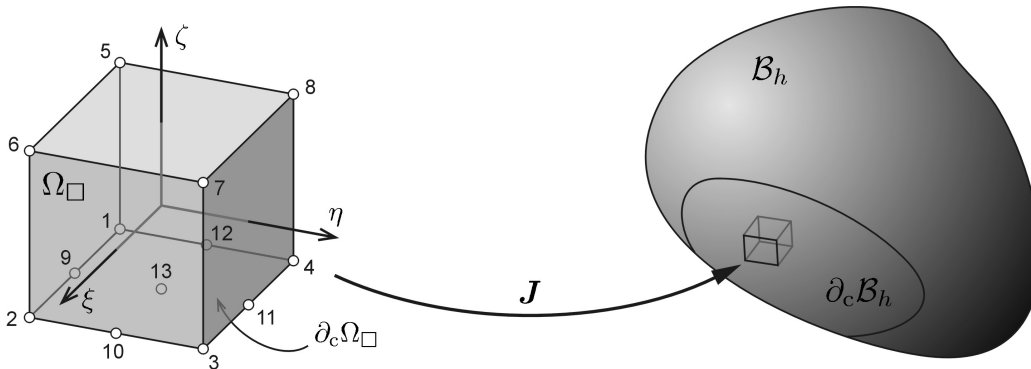


Figure 9: 3D surface enrichment based on p-refinement: 3D enhanced contact element Q1C2 and its map to the current domain.

The standard shape functions for the trilinear quadrilateral with eight nodes are given by

$$N_I^0 = \frac{1}{8}(1 + \xi_I \xi)(1 + \eta_I \eta)(1 + \zeta_I \zeta), \quad I = 1, 2, \dots, 8, \quad (48)$$

where  $(\xi_I, \eta_I, \zeta_I)$  are the corner coordinates of the master brick that are given by the 8 combinations of  $(\pm 1, \pm 1, \pm 1)$ . If this formulation is used for contact we speak of the Q1C1 element.

For the Q1C2 element the shape function at the interior nodes,  $N_5, N_6, N_7$  and  $N_8$ , are the same as above. For the nine surface nodes, standard biquadratic shape functions are used and

multiplied by  $\frac{1}{2}(1 - \zeta)$  to obtain

$$\begin{aligned}
N_1 &= \frac{1}{8}(\xi^2 - \xi)(\eta^2 - \eta)(1 - \zeta) , \\
N_2 &= \frac{1}{8}(\xi^2 + \xi)(\eta^2 - \eta)(1 - \zeta) , \\
N_3 &= \frac{1}{8}(\xi^2 + \xi)(\eta^2 + \eta)(1 - \zeta) , \\
N_4 &= \frac{1}{8}(\xi^2 - \xi)(\eta^2 + \eta)(1 - \zeta) , \\
N_9 &= \frac{1}{4}(1 - \xi^2)(\eta^2 - \eta)(1 - \zeta) , \\
N_{10} &= \frac{1}{4}(\xi^2 + \xi)(1 - \eta^2)(1 - \zeta) , \\
N_{11} &= \frac{1}{4}(1 - \xi^2)(\eta^2 + \eta)(1 - \zeta) , \\
N_{12} &= \frac{1}{4}(\xi^2 - \xi)(1 - \eta^2)(1 - \zeta) , \\
N_{13} &= \frac{1}{2}(1 - \xi^2)(1 - \eta^2)(1 - \zeta) .
\end{aligned} \tag{49}$$

The 13 shape functions of the 3D Q1C2 element satisfy the partition of unity (26) and the compact support property (25). The displacement field within the element then follows from the interpolation

$$\mathbf{u}_e^h = \sum_{I=1}^{13} N_I \mathbf{u}_I . \tag{50}$$

At the contact surface ( $\zeta = -1$ ), shape functions  $N_5$  to  $N_8$  are zero, so that the sum can be simplified. Since each node has three dofs, the 3D Q1C2 element has 39 dofs in total. The internal force vector  $\mathbf{f}_{\text{int}}^e$  and the contact force vector  $\mathbf{f}_c^e$  are easily found as described in Section 2 and Appendix A. If a FE routine is available for the Q1C1 element, the extension to the Q1C2 element is straightforward (see Appendix A).

A transition element is required to connect the Q1C2 element to a Q1 element. Such a transition element, denoted as Q1T2 in the following, consists of a standard 8-node brick element with one additional node along one edge. Without loss of generality, this node is denoted as node 9 and is placed between nodes 1 and 2. The shape functions for node 3 to 8 are the same as for the Q1 element. New are

$$\begin{aligned}
N_1 &= \frac{1}{8}(\xi^2 - \xi)(1 - \eta)(1 - \zeta) , \\
N_2 &= \frac{1}{8}(\xi^2 + \xi)(1 - \eta)(1 - \zeta) , \\
N_9 &= \frac{1}{4}(1 - \xi^2)(1 - \eta)(1 - \zeta) .
\end{aligned} \tag{51}$$

Similar transition elements with one additional node along two or three edges can be constructed. In order to connect the Q1T2 element to the Q1C2 element, a rotation of the Q1T2 element may be required. Instead of employing transition elements one may also use a hanging node technique.

A 3D version of the Q1C4 element can be obtained analogously; it contains 29 nodes (25 nodes in the contact surface and 4 nodes on the top). A 3D version of the Q1CH formulation is more complicated, since the construction of a  $C^1$  continuous surface formulation is not straightforward in 3D. This will be subject of future research.

Static condensation of the enrichment nodes can also be performed in 3D. For that one can first condense the internal nodes (e.g. node 13 for Q1C2) and then loop over all enriched FE edge segments to condense the edge nodes (e.g. nodes 9, 10, 11 and 12 for Q1C2). However, no real advantage is seen in doing this at present.

The number of quadrature points should be increased along with the polynomial. For the application in Section 5.1,  $2 \times 2 \times 2$  Gauss points are used per Q1 element,  $3 \times 3 \times 3$  Gauss points are used for the bulk integral of the Q1C2 element and  $5 \times 5$  Gauss points are used for the surface integral.

## 5 Numerical examples

### 5.1 Peeling of a gecko spatula

The following 3D example considers the peeling behavior of an adhering gecko spatula. Both the new Q1C2 and the standard Q1C1 contact elements are considered and it is seen that the Q1C2 element constitutes a major improvement. The gecko spatula (Figure 10.a) consists of a thin and highly flexible adhesive pad that is about 300 nm long and 200 nm wide but only about 10 nm thick in the middle [29]. The pad is attached to a circular shaft that is about 700 nm long. The geometrical details of the 3D spatula structure are reported in [35] and [36].

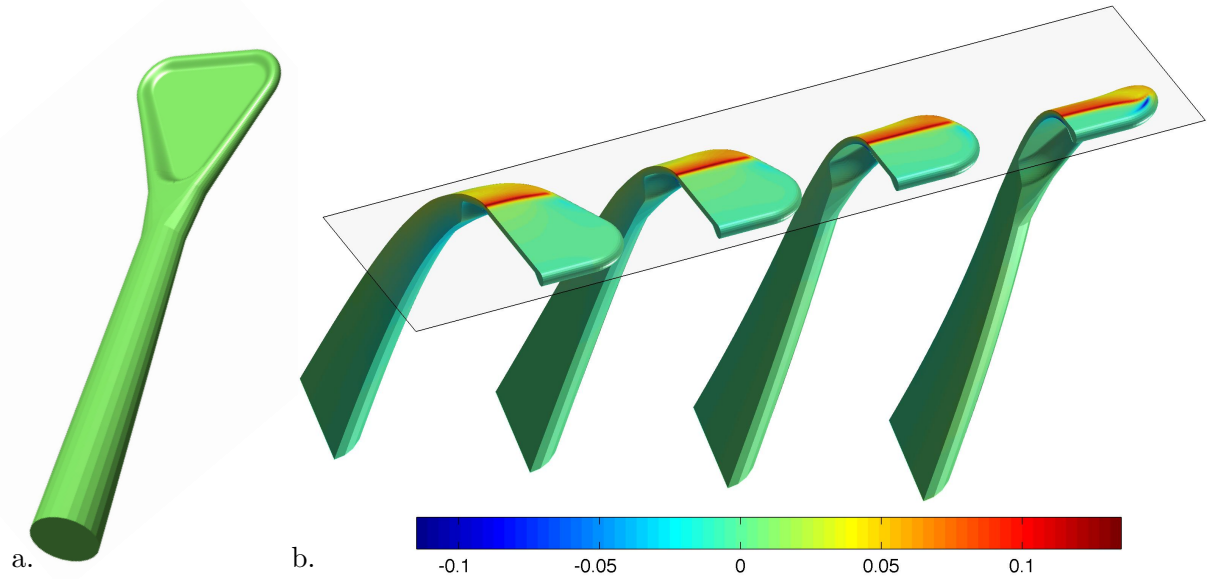


Figure 10: a. Geometry of the gecko spatula; b. Peeling of the spatula showing large stresses at the peeling front. The colors show the stress  $I_1 = \text{tr } \sigma$  normalized by  $E$ .

The spatula is modeled as an isotropic Neo-Hookean solid with  $E = 2$  GPa and  $\nu = 0.2$ . The adhesion of the pad is modeled according to eq. (8) with the parameters  $A_H = 10^{-19}$  J and  $r_0 = 0.4$  nm. The adhesive contact is considered frictionless here. Figure 10.b shows the peeling of the spatula for an applied vertical pull-off force. The inclination of the spatula shaft w.r.t. the peeling plane is kept fixed at  $60^\circ$ . The coloring shows the first stress invariant  $I_1 = \text{tr } \sigma$  of the Cauchy stress tensor. The values range from  $-0.115 E$  (dark blue) to  $0.135 E$  (dark red). On the contact surface of the pad large peeling stresses appear, as is shown in the figure. The largest peeling stresses that occur are  $0.0618 E$  according to eq. (10). The finite element mesh of half the spatula contains about 100,000 brick elements. All elements in the contact surface are considered as Q1Cp elements, the remaining (bulk and surface) elements are Q1 elements. For this mesh, the largest surface diameter of the contact elements is 2.87 nm. Considerable variation of the van der Waals adhesion force occurs over such a distance (see Figure 1). In fact the Q1C1 contact formulation is inappropriate for this mesh and fails to converge during the computation if large displacement increments are used.

Figure 11 shows the load-displacement curve of the peeling process. The white points at 0 nm, 60 nm, 120 nm and 180 nm correspond to the four configurations shown in Figure 10.b. The maximum pull-off force is 6.7 nN which lies within the experimental range observed in [37] and [38]. The enlargement displayed in Figure 11.b shows that the Q1C1 contact formulation is affected by the kind of oscillations observed in the simple 2D example of Section 3.1. The Q1C2

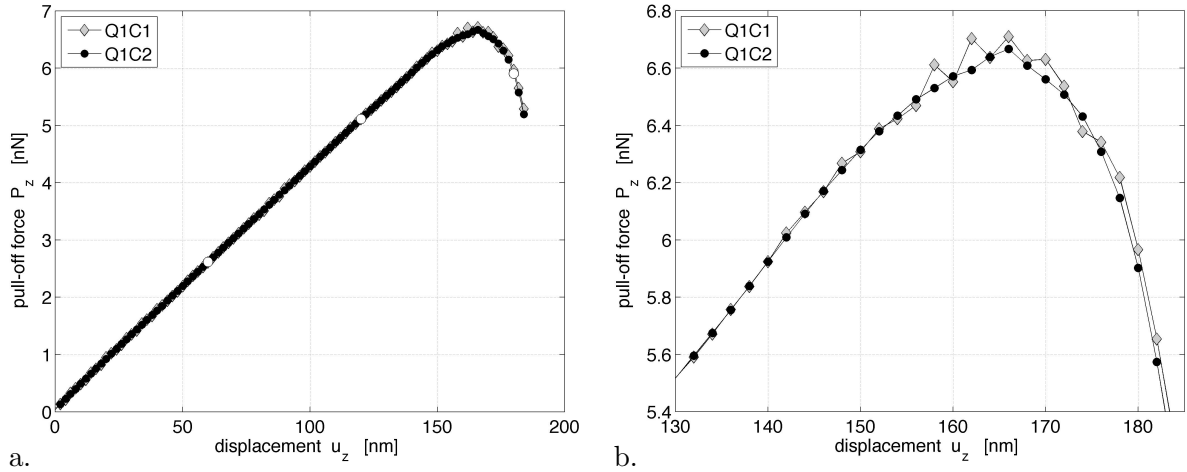


Figure 11: a. Peeling forces for a prescribed vertical displacement of the spatula; b. Enlargement of a.

formulation improves this decisively: The oscillations are reduced significantly (thus increasing the computational accuracy) so that the Newton-Raphson iteration converges faster and the overall simulation runs more stable. The adhesion strength can even be increased by 50%, a case which fails to converge for the Q1C1 formulation. This improvement comes at little numerical extra cost: The number of dofs only increases by 23.5%, as is shown in Table 5. This is still more than 5 times less dofs than for a fully quadratic FE formulation (Q2C2). It

contact formulation	number of FE	dofs
Q1C1	101728 Q1 elements of which 8896 are Q1C1	343242
Q1C2	92664 Q1 elements + 8896 Q1C2 elements + 168 transition elements	423834
Q2C2	101728 Q2 elements	$\approx 2.5 \cdot 10^6$

Table 5: Number of degrees-of-freedom (dofs) for the 3D spatula peeling problem.

is expected that the Q1C4 formulation will produce even smoother results, as would a three-dimensional Q1CH implementation, which is subject of future research. A detailed study of the spatula peeling for different parameters and boundary conditions is considered in [36].

## 5.2 Ironing problem

The enriched contact element formulation is also advantageous for sliding contact computations, which is demonstrated next. Therefore, the frictionless sliding of a rigid cylinder over a soft elastic block is considered, as shown in Figure 12. The radius of the cylinder is  $L_0$  and the block dimensions are  $2L_0 \times 10L_0$ . The bottom surface is fixed in all directions and a periodic boundary condition is applied at the sides. The problem is normalized by the length  $L_0$  and Young's modulus  $E$ . Poisson's ratio is chosen as  $\nu = 0.3$ . Plane strain conditions are considered, such that the computation can be performed in 2D. In each dimension, four elements are used along  $L_0$ . Contact is modeled by the penalty method according to eq. (13) using a normalized penalty

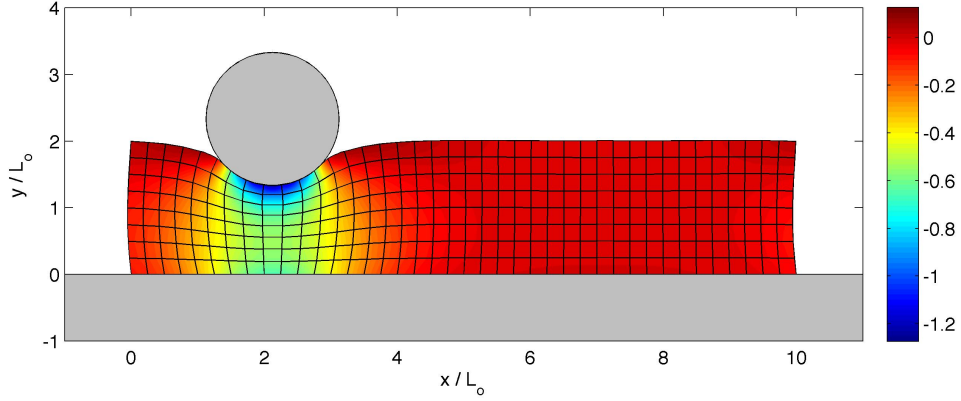


Figure 12: Ironing problem: frictionless sliding contact between a rigid cylinder and a soft block. The coloring shows the stress  $I_1 = \text{tr } \boldsymbol{\sigma}$  normalized by  $E$ .

parameter of  $\epsilon_n = 100$  (i.e. normalized by  $E/L_0$ ). A similar sliding example is considered in [39] and [40].

The cylinder is pressed into the block by imposing a vertical displacement of  $2/3 L_0$ . Keeping the vertical displacement constant, a horizontal displacement is then applied to the cylinder. Figure 13 shows the net contact forces  $P_x$  and  $P_y$  as a function of the horizontal sliding distance. In theory, the horizontal contact force should be identically zero, while the vertical contact force

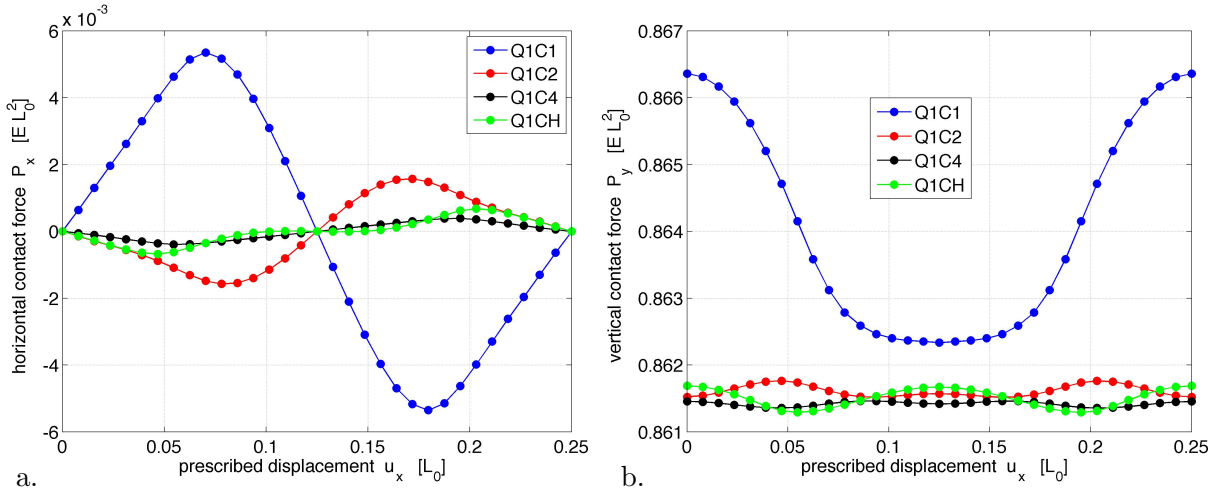


Figure 13: Net contact force between cylinder and block in dependance of the sliding distance  $u_x$ : a. Horizontal contact force  $P_x$ ; b. Vertical contact force  $P_y$ .

should be constant. Numerically, both force components oscillate about a mean value with the wavelength  $L_0/4$  (i.e. the length of one finite element). As Figure 13 shows, the oscillations reduce significantly for the new enhanced contact formulations. Table 6 lists the amplitudes of  $P_x$  and  $P_y$ . One can observe that the oscillation in  $P_x$  are reduced by a factor of 3 for the Q1C2 formulation, by a factor of 8 for the Q1CH formulation and by a factor of 13 for Q1C4 formulation. 100 equidistant quadrature points are used to evaluate the contact integral (17) to high accuracy for each element. The improvement obtained by the new contact elements is quite similar to the improvement observed during peeling (see Figure 8). According to Figure 13,

element	$\Delta P_x$	$\Delta P_y$	ave( $P_y$ )
Q1C1	$1.0706 \cdot 10^{-2}$	$4.0265 \cdot 10^{-3}$	0.86401
Q1C2	$3.1447 \cdot 10^{-3}$	$2.4368 \cdot 10^{-4}$	0.86161
Q1C4	$7.8114 \cdot 10^{-4}$	$1.0326 \cdot 10^{-4}$	0.86142
Q1CH	$1.3626 \cdot 10^{-3}$	$3.9694 \cdot 10^{-4}$	0.86150

Table 6: Performance of the enhanced contact elements for the frictionless ironing example (see Figure 12).

formulation Q1C4 performs better than the Q1CH formulation.

Figure 14 shows an enlargement of the contact deformation and stress<sup>8</sup> for the original Q1C1 formulation and the three new enrichment formulations Q1C2, Q1C4 and Q1CH. The stress

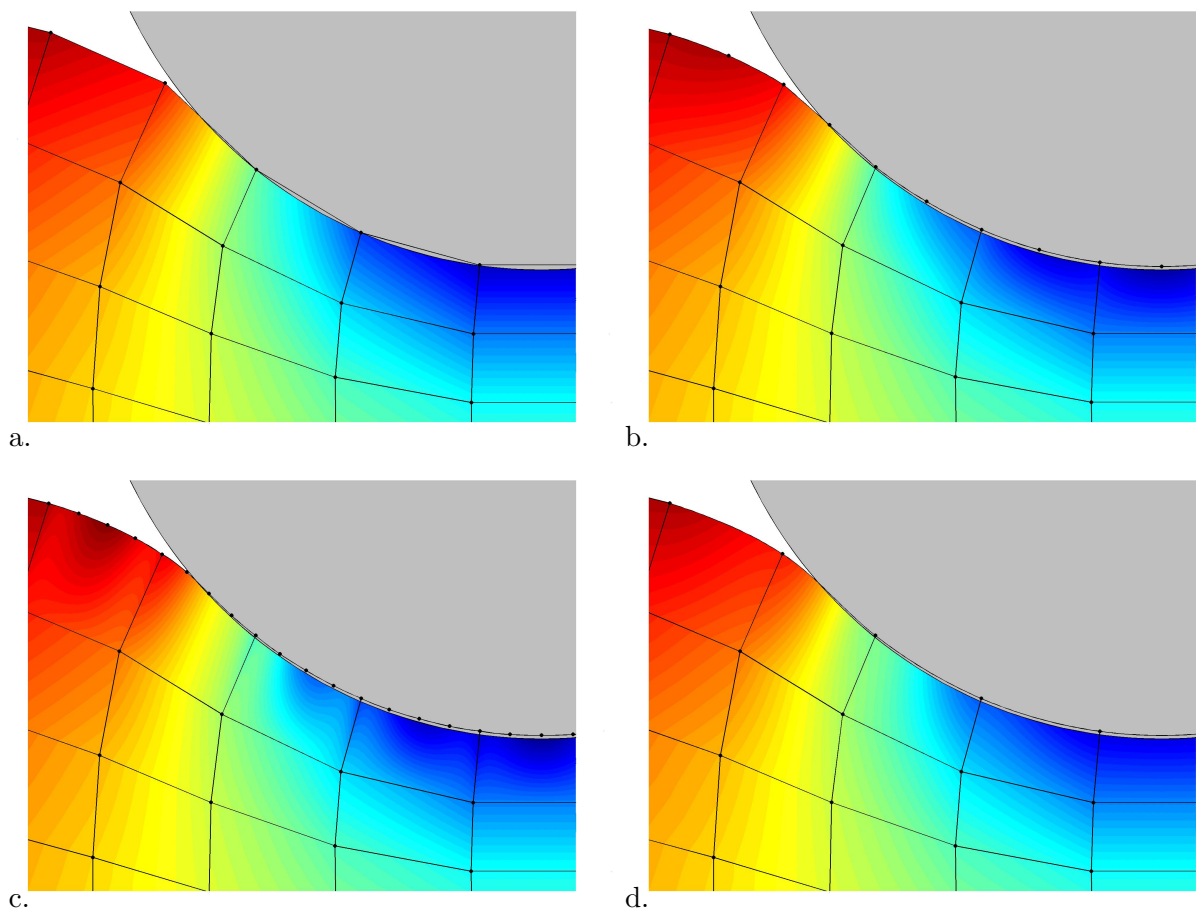


Figure 14: Enlargement of the contact deformation and  $I_1$  stress according to the: a. Q1C1 formulation; b. Q1C2 formulation.; c. Q1C4 formulation; d. Q1CH formulation.

coloring for these four enlargements is the same as shown in Figure 12. Enlargement (a) shows the poor surface approximation achieved for the Q1C1 formulation. In contrast, the Q1C2 formulation performs much better. Close observation, however, shows that the surface has kinks, i.e. the deformation is not  $C^1$  as is the case for the Q1CH formulation shown in enlargement (d).

<sup>8</sup>The stress field is generated from interpolating the nodal stress values, which in turn are obtained from a least square minimization of the error between interpolated stresses and quadrature point stresses.

Close inspection of the Q1C4 result (enlargement (c)) reveals oscillations in the stress field. Such oscillations are characteristic for high order polynomial interpolations. They indicate that the polynomial degree should not be chosen too large.

As a final consideration, the pressure distribution between the contacting bodies is examined, as it is defined by eq. (13). This is shown in Figure 15 for the four different contact element formulations. It is seen that the original Q1C1 formulation yields a highly inaccurate and

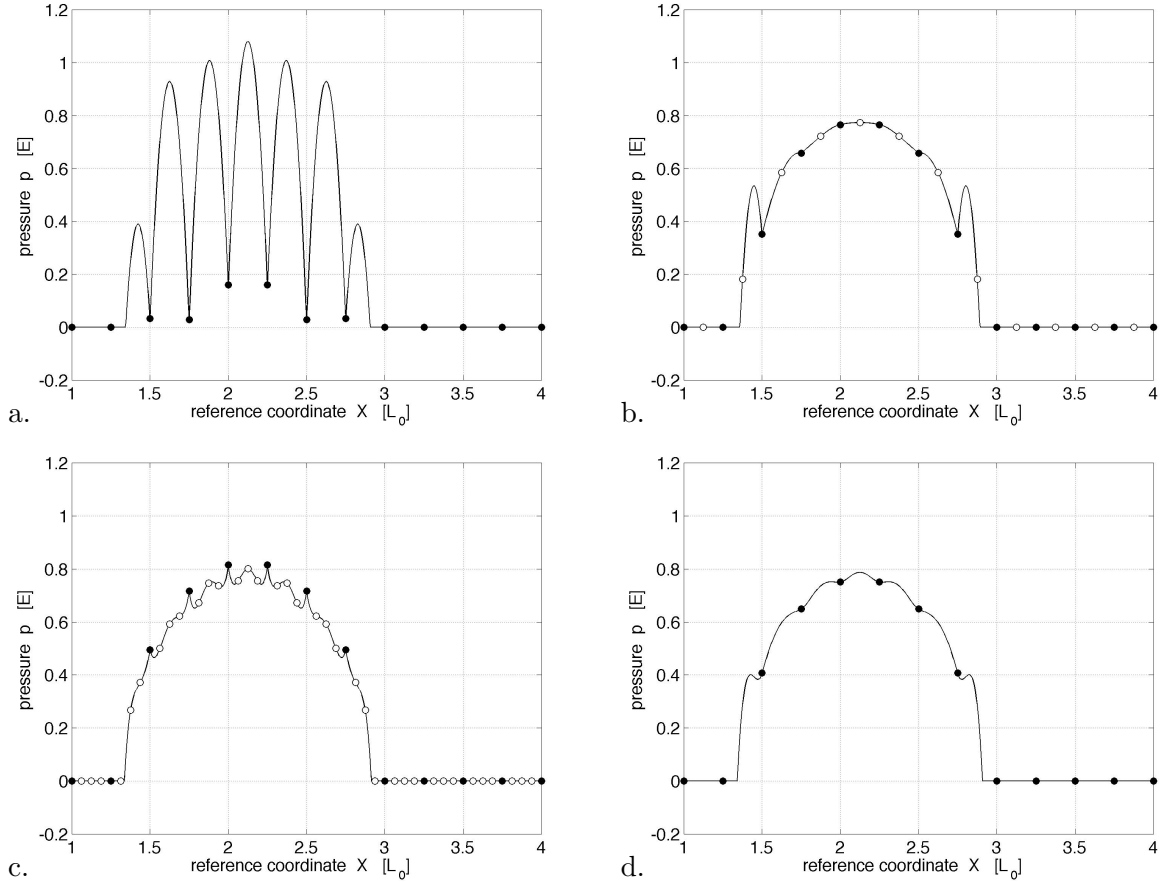


Figure 15: Contact pressure according to the: a. Q1C1 formulation; b. Q1C2 formulation.; c. Q1C4 formulation; d. Q1CH formulation. The dark dots show the pressure at the standard FE nodes, the white dots show the pressure at the enrichment nodes.

oscillatory pressure field.<sup>9</sup> The accuracy improves considerably for the enriched contact elements Q1C2, Q1C4 and Q1CH. In terms of smoothness, the Q1CH formulation provides the best results. In the figure, the black dots mark the pressure at the FE corner nodes, while the white dots mark the pressure at the enriched FE nodes. The configuration considered here is the same as the one shown in Figure 12 and 14. It should be noted that the actual distribution of the pressure has a somewhat limited significance, since, numerically, equilibrium is only enforced for the nodal averages obtained from integration (15).

In view of the behavior observed in Figures 13, 14 and 15, and in view of the results obtained in Section 3.4.2, we conclude that the enhanced Q1CH formulation performs best.

<sup>9</sup>If one only considers the nodal values, or the elemental midpoints, as is sometimes done, the pressure will appear much smoother.

## 6 Conclusion

During peeling sharp stresses can appear at the peeling front, which cause considerable difficulties in standard FE contact formulations. This paper provides an improved contact formulation, that is efficient, simple and effective. The formulation is based on the enrichment of the contact surface description at the element level in order to improve the evaluation and integration of the contact forces, even for coarse FE meshes. Thus, a class of new enhanced contact finite elements is developed, using two different enrichment techniques: The first consists of a p-refinement of the contact surface, and the associated new contact element is denoted as Q1C $p$  element, where  $p = 1, 2, 4$  have been considered. This idea is formulated both in 2D and 3D. The second technique consists of an Hermite enrichment, which is  $C^1$  on the contact surface but  $C^0$  elsewhere, and the associated contact element is denoted as Q1CH element. The new elements show a major improvement in peeling and sliding computations, as is demonstrated by several numerical examples. Among those is the peeling computation of a gecko spatula. The examples indicate that the Q1CH element performs best among the new enriched contact elements.

For future work, several extensions are planned. The first major extension is to formulate and implement a three-dimensional version of the Q1CH contact element. Such an element requires a  $C^1$  continuous 3D surface description, which is not straightforward to develop. The expected benefit will be a highly efficient and accurate contact formulation. Further considerations are the extension to frictional contact and the extension to contact between deformable bodies.

## Acknowledgements

The author is grateful to the German Research Foundation (DFG) for supporting this research under project SA1822/5-1, and also thanks the student Katrin Nagel for her help in analyzing the peeling test case.

## A Outline of the FE bulk equations for the enriched elements

Within a finite element, the deformation  $\mathbf{x} = \mathbf{X} + \mathbf{u}$  is approximated by the interpolation

$$\mathbf{x}_e^h = \sum_{I=1}^{n_{\text{en}}} N_I \mathbf{x}_I, \quad (52)$$

where  $N_I$  are the shape functions of the element and  $n_{\text{en}}$  is the number of element nodes, which is  $n_{\text{en}} = 4$  for Q1C1,  $n_{\text{en}} = 5$  for Q1C2,  $n_{\text{en}} = 6$  for Q1CH or  $n_{\text{en}} = 7$  for Q1C4 in 2D and  $n_{\text{en}} = 8$  (Q1C1),  $n_{\text{en}} = 13$  (Q1C2),  $n_{\text{en}} = 9$  (Q1T2) or  $n_{\text{en}} = 29$  (Q1C4) in 3D, respectively. The interpolation of  $\mathbf{X}_e^h$  and  $\mathbf{u}_e^h$  is analogous. The deformation gradient  $\mathbf{F}_e$ , corresponding to  $\mathbf{x}_e^h$ , can be obtained from the inversion of

$$\frac{\partial \mathbf{X}}{\partial \mathbf{x}} \approx \mathbf{F}_e^{-1} = \sum_{I=1}^{n_{\text{en}}} \mathbf{X}_I \otimes \nabla_{\mathbf{x}} N_I, \quad (53)$$

where  $\nabla_{\mathbf{x}} N_I$  denotes the gradient of shape function  $N_I$  w.r.t.  $\mathbf{x}$ , which can be obtained through

$$\nabla_{\mathbf{x}} N_I = \mathbf{J}_e^{-T} \nabla_{\boldsymbol{\xi}} N_I, \quad (54)$$

where

$$\frac{\partial \mathbf{x}}{\partial \boldsymbol{\xi}} \approx \mathbf{J}_e = \sum_{I=1}^{n_{\text{en}}} \mathbf{x}_I \otimes \nabla_{\boldsymbol{\xi}} N_I \quad (55)$$

is the deformation gradient between master element and the current element configuration and where  $\nabla_{\boldsymbol{\xi}} N_I$  denotes the vector of derivatives  $N_{I,\xi}$ ,  $N_{I,\eta}$  and  $N_{I,\zeta}$ , which can be easily obtained from the shape functions given in Sections 3.2, 3.3 and 4. The Cauchy stress tensor follows from the constitutive law. In this paper a Neo-Hookean material model is considered in the form

$$\boldsymbol{\sigma} = \frac{\Lambda}{J} \ln J \mathbf{I} + \frac{\mu}{J} (\mathbf{F}\mathbf{F}^T - \mathbf{I}) , \quad (56)$$

where  $J = \det \mathbf{F}$ . Given  $\nabla_{\mathbf{x}} N_I$ , the B-Matrix  $\mathbf{B}_e = [\mathbf{B}_1 \ \mathbf{B}_2 \ \cdots \ \mathbf{B}_{n_{\text{en}}}]$  is formed by the blocks

$$\mathbf{B}_I = \begin{bmatrix} N_{I,x_1} & 0 & 0 \\ 0 & N_{I,x_2} & 0 \\ 0 & 0 & N_{I,x_3} \\ 0 & N_{I,x_3} & N_{I,x_2} \\ N_{I,x_3} & 0 & N_{I,x_1} \\ N_{I,x_2} & N_{I,x_1} & 0 \end{bmatrix} . \quad (57)$$

The internal force vector then follows as

$$\mathbf{f}_{\text{int}}^e = \int_{\Omega_{\square}} \mathbf{B}_e^T \boldsymbol{\sigma} \det \mathbf{J} \, d\Omega , \quad (58)$$

which is in the same form as for standard displacement-based finite elements. The dimension of  $\mathbf{f}_{\text{int}}^e$  is  $(3n_{\text{en}} \times 1)$  in 3D. Also the stiffness matrix is in the usual form and can be found in [33].

## B Implementation remarks on the Q1CH element

In the FE implementation of the Q1CH element, it is convenient to use the nodal variable  $\mathbf{u}_{I,\xi}$  within the element routine and variable  $\mathbf{u}_{I,S}$  outside of the element routine. They are related according to

$$\mathbf{u}_{I,\xi} = S_{,\xi} \mathbf{u}_{I,S} , \quad (59)$$

with

$$S_{,\xi} := \frac{\partial S}{\partial \xi} = \frac{L_c}{2} \quad (60)$$

in 2D. Here  $L_c$  is the contact element length, i.e., the surface distance between nodes 1 and 2 in the reference configuration. It is emphasized, that the contact elements do not need to be equidistant across the mesh. If they are not equidistant, one simply has different values for  $\mathbf{u}_{I,\xi}$  between adjacent elements, which does not pose any difficulties.

The force vector and tangent matrix of the Q1CH element are computed as specified in Appendix A. These two arrays now refer to the  $\mathbf{u}_{I,\xi}$  system and thus need to be transformed back to the  $\mathbf{u}_{I,S}$  system, which is used outside the element. The components of the displacement vector  $\mathbf{u}$  are therefore grouped according to

$$\mathbf{u} = \begin{bmatrix} \mathbf{u}_N \\ \mathbf{u}_{,S} \end{bmatrix} , \quad (61)$$

where  $\mathbf{u}_N$  contains all nodal displacements  $\mathbf{u}_I$  ( $I = 1, \dots, 4$ ) and  $\mathbf{u}_{,S}$  contains all nodal displacement derivatives  $\mathbf{u}_{I,S}$  ( $I = 1, 2$ ). These are transformed according to eq. (59), so that we can denote

$$\mathbf{u}_{,\xi} := S_{,\xi} \mathbf{u}_{,S} \quad (62)$$

as the vector that contains all nodal displacement derivatives  $\mathbf{u}_{I,\xi}$ . Note that  $S_\xi$  can change between elements.

The Newton-Raphson method is used to solve equilibrium iteratively. At each iteration step the matrix equation  $\mathbf{k} \Delta \mathbf{u} = -\mathbf{f}$  is solved for the displacement increment  $\Delta \mathbf{u}$ . According to definition (61) we write

$$\begin{bmatrix} \mathbf{k}_{NN} & \mathbf{k}_{N,S} \\ \mathbf{k}_{,SN} & \mathbf{k}_{,S,S} \end{bmatrix} \begin{bmatrix} \Delta \mathbf{u}_N \\ \Delta \mathbf{u}_{,S} \end{bmatrix} = - \begin{bmatrix} \mathbf{f}_N \\ \mathbf{f}_{,S} \end{bmatrix} \quad (63)$$

in the  $\mathbf{u}_{I,S}$  system or

$$\begin{bmatrix} \mathbf{k}_{NN} & \mathbf{k}_{N,\xi} \\ \mathbf{k}_{,\xi N} & \mathbf{k}_{,\xi,\xi} \end{bmatrix} \begin{bmatrix} \Delta \mathbf{u}_N \\ \Delta \mathbf{u}_{,\xi} \end{bmatrix} = - \begin{bmatrix} \mathbf{f}_N \\ \mathbf{f}_{,\xi} \end{bmatrix} \quad (64)$$

in the  $\mathbf{u}_{I,\xi}$  system. According to eq. (62) this yields the following relations at the element level between the force vector and stiffness matrix contributions:

$$\mathbf{f}_{,S}^e = S_{,\xi} \mathbf{f}_{,\xi}^e, \quad (65)$$

$$\mathbf{k}_{N,S}^e = S_{,\xi} \mathbf{k}_{N,\xi}^e, \quad (66)$$

$$\mathbf{k}_{,SN}^e = S_{,\xi} \mathbf{k}_{,\xi N}^e, \quad (67)$$

$$\mathbf{k}_{,S,S}^e = S_{,\xi}^2 \mathbf{k}_{,\xi,\xi}^e. \quad (68)$$

In the implementation of the Q1CH element we then proceed as follows: At the start of the element routine, we transform the element displacement vector to the  $\xi$ -system according to eq. (62). We then compute the force and stiffness arrays in the  $\xi$ -system, and transform them back into the  $S$ -system according to eqs. (65)–(68). Outside the element we only work in the  $S$ -System.

## References

- [1] Wei Y, Hutchinson JW. Interface strength, work of adhesion and plasticity in the peel test. *Int. J. Fracture* 1998; **93**:315–333.
- [2] Crisfield MA, Alfano G. Adaptive hierarchical enrichment for delamination fracture using a decohesive zone model. *Int. J. Numer. Meth. Engrg.* 2002; **54**(9):1369–1390.
- [3] Diehl T. On using a penalty-based cohesive-zone finite element approach, Part I: Elastic solution benchmarks. *Int. J. Adhesion Adhesives* 2008; **28**:237–255.
- [4] De Lorenzis L, Zavarise G. Modeling of mixed mode debonding in the peel test applied to superficial reinforcements. *Int. J. Solids Struc.* 2008; **45**:5419–5436.
- [5] Puso MA, Laursen TA, Solberg J. A segment-to-segment mortar contact method for quadratic elements and large deformations. *Comput. Methods Appl. Mech. Engrg.* 2008; **197**:555–566.
- [6] Simo JC, Armero F. Geometrically non-linear enhanced strain mixed methods and the method of incompatible modes. *Int. J. Numer. Meth. Engrg.* 1992; **33**:1413–1449.
- [7] Belytschko T, Moes N, Usui S, Parimi C. Arbitrary discontinuities in finite elements. *Int. J. Numer. Meth. Engrg.* 2001; **50**:993–1013.
- [8] Laursen TA. *Computational Contact and Impact Mechanics: Fundamentals of modeling interfacial phenomena in nonlinear finite element analysis*. Springer, 2002.

- [9] Wriggers P. *Computational Contact Mechanics*. 2<sup>nd</sup> edn., Springer, 2006.
- [10] Sauer RA, Li S. A contact mechanics model for quasi-continua. *Int. J. Numer. Meth. Engrg.* 2007; **71**(8):931–962.
- [11] Hansson E, Klarbring A. Rigid contact modelled by CAD surface. *Eng. Comput.* 1990; **7**:344–348.
- [12] El-Abbasi N, Meguid SA, Czekanski A. On the modeling of smooth contact surfaces using cubic splines. *Int. J. Numer. Meth. Engrg.* 2001; **50**:953–967.
- [13] Padmanabhan V, Laursen TA. A framework for development of surface smoothing procedures in large deformation frictional contact analysis. *Finite Elem. Anal. Des.* 2001; **37**:173–198.
- [14] Wriggers P, Krstulovic-Opara L, Korelc J. Smooth  $C^1$ -interpolations for two-dimensional frictional contact problems. *Int. J. Numer. Meth. Engrg.* 2001; **51**:1469–1495.
- [15] Stadler M, Holzapfel GA, Korelc J.  $C^n$  continuous modelling of smooth contact surfaces using NURBS and application to 2D problems. *Int. J. Numer. Meth. Engrg.* 2003; **57**:2177–2203.
- [16] Chamoret D, Saillard P, Rassineux A, Bergheau JM. New smoothing procedures in contact mechanics. *J. Comput. Appl. Math.* 2004; **168**:107–116.
- [17] Pietrzak G, Curnier A. A continuum mechanics modeling and augmented Lagrange formulation of multibody, large deformation frictional contact problems. *Proceedings of COM-PLAS 5*, Owen DR, Hinton E, Oñate E (eds.), CIMNE, Barcelona, 1997; 878–883.
- [18] Krstulovic-Opara L, Wriggers P, Korelc J. A  $C^1$ -continuous formulation for 3D finite deformation friction contact. *Comp. Mech.* 2002; **29**:27–42.
- [19] Puso MA, Laursen TA. A 3D contact smoothing method using Gregory patches. *Int. J. Numer. Meth. Engrg.* 2002; **54**:1161–1194.
- [20] Cottrell JA, Hughes TJR, Bazilevs Y. *Isogeometric Analysis*. Wiley, 2009.
- [21] Franke D, Düster A, Nübel V, Rank E. A comparison of the h-, p-, hp- and rp-version of the FEM for the solution of the 2D Hertzian contact problem. *Comput. Mech.* 2010; **45**:513–522.
- [22] Konyukhov A, Schweizerhof K. Incorporation of contact for high-order finite elements in covariant form. *Comput. Methods Appl. Mech. Engrg.* 2009; **198**:1213–1223.
- [23] Samimi M, van Dommelen JAW, Geers MGD. An enriched cohesive zone model for delamination in brittle interfaces. *Int. J. Numer. Meth. Engrg.* 2009; **80**(5):609–630.
- [24] Guiamatsia I, Ankersen JK, Davies GAO, Iannucci L. Decohesion finite element with enriched basis functions for delamination. *Compos. Sci. Technol.* 2009; **69**(15-16):2616–2624.
- [25] Xu XP, Needleman A. Numerical simulations of fast crack growth in brittle solids. *J. Mech. Phys. Solids* 1994; **42**(9):1397–1434.
- [26] Sauer RA, Li S. An atomic interaction-based continuum model for adhesive contact mechanics. *Finite Elem. Anal. Des.* 2007; **43**(5):384–396.

- [27] Sauer RA, Wriggers P. Formulation and analysis of a 3D finite element implementation for adhesive contact at the nanoscale. *Comput. Methods Appl. Mech. Engrg.* 2009; **198**:3871–3883.
- [28] Sauer RA. Computational contact formulations for soft body adhesion. *Advances in Soft Matter Mechanics*, Li S, Sun B (eds.), Springer, 2012.
- [29] Tian Y, Pesika N, Zeng H, Rosenberg K, Zhao B, McGuiggan P, Autumn K, Israelachvili J. Adhesion and friction in gecko toe attachment and detachment. *Proc. Natl. Acad. Sci. USA* 2006; **103**(51):19 320–19 325.
- [30] Sauer RA. A computational contact model for nanoscale rubber adhesion. *Constitutive Models for Rubber VI*, Heinrich G, Kaliske M, Lion A, Reese S (eds.), Taylor & Francis Group, 2009; 47–52.
- [31] Hughes TJR. *The Finite Element Method*. Dover, 2000.
- [32] Braess D. *Finite elements – Theory, fast solvers, and applications in solid mechanics*. 2<sup>nd</sup> edn., Cambridge University Press, 2001.
- [33] Wriggers P. *Nonlinear Finite Element Methods*. Springer, 2008.
- [34] Sauer RA. The peeling behavior of thin films with finite bending stiffness and the implications on gecko adhesion. *J. Adhes.* 2011; **87**(7-8):624–643.
- [35] Sauer RA. Multiscale modeling and simulation of the deformation and adhesion of a single gecko seta. *Comp. Meth. Biomech. Biomed. Engrg.* 2009; **12**(6):627–640.
- [36] Sauer RA, Holl M. A detailed 3D finite element analysis of the peeling behavior of a gecko spatula. *Comp. Meth. Biomech. Biomed. Engrg.* 2012; **DOI: 10.1080/10255842.2011.628944**.
- [37] Huber G, Mantz H, Spolenak R, Mecke K, Jacobs K, Gorb SN, Arzt E. Evidence for capillarity contributions to gecko adhesion from single spatula nanomechanical measurements. *Proc. Natl. Acad. Sci. USA* 2005; **102**(45):16 293–16 296.
- [38] Sun W, Neuzil P, Kustandi TS, Oh S, Samper D. The nature of the gecko lizard adhesive force. *Biophys. J.* 2005; **89**(2):L14–L17.
- [39] Yang B, Laursen TA, Meng X. Two dimensional mortar contact methods for large deformation frictional sliding. *Int. J. Numer. Meth. Engrg* 2005; **62**:1183–1225.
- [40] Fischer KA, Wriggers P. Mortar based frictional contact formulation for higher order interpolations using the moving friction cone. *Comput. Methods Appl. Mech. Engrg.* 2006; **195**:5020–5036.